Available online at www.sciencedirect.com

SciVerse ScienceDirect

Acta Materialia 60 (2012) 4005–4016

Acta MATERIALIA

www.elsevier.com/locate/actamat

Evolution of strength and microstructure during annealing of heavily cold-drawn 6.3 GPa hypereutectoid pearlitic steel wire

Y.J. Li [a,b,*], P. Choi [b], S. Goto [c], C. Borchers [a], D. Raabe [b,*], R. Kirchheim [a,b]

[a] Institut für Materialphysik, Georg-August-Universität Göttingen, Friedrich-Hund-Platz 1, D-37077 Göttingen, Germany
[b] Max-Planck Institut für Eisenforschung, Max-Planck-Str. 1, D-40237 Düsseldorf, Germany
[c] Department of Materials Science and Engineering, Faculty of Engineering and Resource Science, Akita University, Tegata Gakuencho, Akita 010-0852, Japan

Received 28 January 2012; received in revised form 1 March 2012; accepted 3 March 2012

Abstract

Hypereutectoid steel wires with 6.35 GPa tensile strength after a cold-drawing true strain of 6.02 were annealed between 300 and 723 K. The ultrahigh strength remained upon annealing for 30 min up to a temperature of 423 K but dramatically decreased with further increasing temperature. The reduction of tensile strength mainly occurred within the first 2–3 min of annealing. Atom probe tomography and transmission electron microscopy reveal that the lamellar structure remains up to 523 K. After annealing at 673 K for 30 min, coarse hexagonal ferrite (sub)grains with spheroidized cementite, preferentially located at triple junctions, were observed in transverse cross-sections. C and Si segregated at the (sub)grain boundaries, while Mn and Cr enriched at the ferrite/cementite phase boundaries due to their low mobility in cementite. No evidence of recrystallization was found even after annealing at 723 K for 30 min. The stability of the tensile strength for low-temperature annealing (<473 K) and its dramatic drop upon high-temperature annealing (>473 K) are discussed based on the nanostructural observations.

Keywords: Pearlitic steel; Ultrahigh strength; Atom probe tomography; Annealing; Grain boundary segregation

1. Introduction

Cold-drawn, hypereutectoid pearlitic steel wires show maximal tensile strength above 5 GPa [1], thus making them the strongest bulk nanostructured materials. Although pearlite has a large potential in engineering applications, the microstructural origin of its extreme strength is not well understood. It has been shown by several authors that cold drawing not only strengthens pearlite by refining the lamellae structure [2–5], but also simultaneously causes partial chemical decomposition of cementite [6–18] and a structural transition from crystalline to amorphous cementite [9,13,14]. The deformation-induced decomposition and microstructural change of cementite is closely related to several other phenomena, such as a strong redistribution of carbon and other alloy elements like Si and Mn in both cementite and ferrite; a variation of the deformation accommodation at the phase interfaces due to a change in the carbon concentration gradient at the interfaces; mechanical alloying; and a further reduction of the deformability of cementite when rendered amorphous. Since these phenomena occur at the atomic scale, the understanding of the strengthening mechanisms of cold-drawn hypereutectoid pearlitic wires can only be improved on the basis of atomic-scale investigations.

Taking a first step in this direction, we recently studied the redistribution of carbon in ferrite and cementite in ultrahigh-strength pearlitic steel wires for a wide range of (true) drawing strains between 0 and 6.02 using atom probe

---

[*] Corresponding authors. Address: Max-Planck Institut für Eisenforschung, Max-Planck-Str. 1, D-40237 Düsseldorf, Germany. Tel.: +49 211 6792853; fax: +49 211 6792333.

E-mail addresses: y.li@mpie.de (Y.J. Li), d.raabe@mpie.de (D. Raabe), rkirch@ump.gwdg.de (R. Kirchheim).

1359-6454/$36.00 © 2012 Acta Materialia Inc. Published by Elsevier Ltd. All rights reserved.
http://dx.doi.org/10.1016/j.actamat.2012.03.006

tomography (APT) [17,18]. In ferrite, we found that the carbon concentration increases with the drawing strain up to 3.47 and then saturates with further deformation. We found evidence of the formation of dislocation (sub)-grain boundaries in the ferrite lamellae and observed the segregation of carbon at ferrite dislocations and (sub)grain boundaries. In cementite, we found that the carbon concentration decreases with the thickness of the cementite lamellae. This finding gives a quantitative correlation between plastic deformation and cementite decomposition in cold-drawn pearlitic steel wires [17,18]. Furthermore, both the saturation of the carbon content in the ferrite and the discontinuation of further decomposition of cementite at high strains indicate the important role of dislocations during cementite decomposition. This is also supported by the direct observation of carbon segregation at ferrite dislocations and grain boundaries [17,18].

Nanostructured materials produced by severe plastic deformation are highly susceptible to grain coarsening upon heating, due to the large density of dislocations and grain boundaries. However, little attention has been paid so far to the thermal stability of the nanostructure of heavily cold-deformed pearlitic wires [9,19–21] and its effect on the mechanical properties. In this work, we study the changes in the nanostructure of a heavily cold-drawn hypereutectoid pearlitic steel wire upon annealing in order to elucidate the mechanism leading to the ultrahigh strength of cold-drawn pearlitic steel wires. The wires studied here were subjected to the most extreme deformation by cold drawing to a true drawing strain of $\epsilon = 6.02$ and exhibit the highest tensile strength achieved to date (6.35 GPa). The tensile strength was measured as a function of the annealing temperature between 423 and 723 K and of the annealing time. The samples were characterized by means of APT in conjunction with transmission electron microscopy (TEM). APT yields three-dimensional elemental maps with near-atomic resolution. This technique is a key to the current study as it allows us to identify the carbon distribution in the drawn and heat-treated pearlite samples [16,22–28]. A local electrode atom probe (LEAP 3000X HR$^{\mathrm{TM}}$, Cameca Instruments) was used, which provides a larger field of view, faster data acquisition rates and higher mass resolution [29–32] compared to conventional atom probes and thus yields compositional data with high accuracy. We surprisingly observed hexagonal (sub)grains in ferrite after annealing, where carbon is segregated to (sub)grain boundaries and spheroidized cementite particles are preferentially located at triple junctions. In addition, the redistribution of other alloying elements, such as Si, Mn and Cr, upon annealing is also quantified and discussed from the viewpoint of the kinetic barriers in terms of the differences in diffusion coefficients between the two abutting phases (ferrite and cementite). On the basis of our experimental observations, we discuss the influence of annealing temperature T and time, and also of the alloying elements and their respective redistribution on the drop in tensile strength upon heat treatment.

2. Experimental

2.1. Material and experimental methods

The material studied in this work was a pearlitic steel wire of hypereutectoid composition (Fe–0.98C–0.31Mn–0.20Si–0.20Cr–0.01Cu–0.006P–0.007S in wt.% and Fe–4.40C–0.30Mn–0.39Si–0.21Cr–0.003Cu–0.01P–0.01S in at.%), provided by Suzuki Metal Industry Co., Ltd. The as-deformed wires were in a cold-drawn state, with a true strain of $\epsilon = 6.02$. Samples taken from this material were annealed for 30 min between 423 and 723 K, at 50 K intervals. Tensile strength, APT and TEM measurements were taken on the as-deformed and annealed wires. The tensile strength was measured with a Dia Stron LEX 810 device using an initial strain rate of $\dot{\epsilon_0} = 1.16 \times 10^{-3}\ \mathrm{s}^{-1}$.

The local electrode atom probe was used to analyze the nanostructural changes and the three-dimensional (3-D) elemental distributions upon annealing. The measurements were performed in voltage mode at 70 K, with a pulse fraction of 15%, a pulse repetition rate of 200 kHz and a detection rate of 0.005 atoms per pulse. APT samples perpendicular to the wire axis were prepared using a dual-beam focused ion beam (FEI Helios NanoLab 600TM) according to the procedure described in Ref. [15]. Reconstructions of the APT data were made using standard parameters for the image compression factor (1.65) and the evaporation field (33 V nm^{-1}), with an efficiency of the detector of 0.37. The final specimen tip radii (after APT measurements) were also taken into account for the reconstructions. TEM samples were prepared using the focused ion beam lift-out method. The sample preparation was done with 30 kV Ga ions, finishing the last step with 5 kV Ga ions. We used a Philips CM30 instrument at an acceleration voltage of 300 kV.

2.2. Mass spectrum analyses of atom probe data

The assignment of ion peaks in a mass spectrum of cold-drawn pearlitic steel wire has been addressed previously [8,15,18]. A mass spectrum of an annealed wire with an initial drawing strain of 6.02 is shown in Fig. 1a. All peaks due to Fe, alloy elements (C, Si, Cr and Mn) as well as impurities like P and S are assigned. As reported in Refs. [17,18] for cold-drawn wires, the mass spectra of ferrite (Fig. 1b) and cementite (Fig. 1c) also reveal the presence of the peak at 24.5 Da in cementite only, which means that 100% of the peak at 24 Da is due to C_2^+ in the ferrite, while a mixture of ions from C_2^+ and C_4^{2+} in the cementite contribute to this peak. A peak deconvolution algorithm (supplied by the software IVAS, Cameca Instruments) taking into account the isotope ratios of C was applied to the peak at m/n = 24 Da. The result shows that less than 50% of the peak is due to C_4^{2+} in the cementite, while for the cold-drawn wires the contribution from C_4^{2+} exceeds 80% [17]. It is reported that the fractions of carbon molecular ions change with the APT acquisition conditions, e.g. temperature,

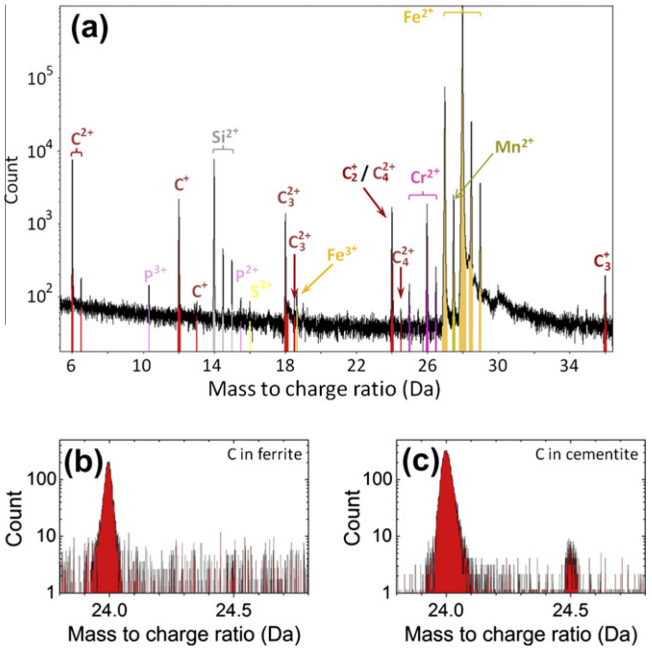

Fig. 1. (a) Mass spectrum of a cold-drawn ($\epsilon = 6.02$) wire after annealing at 673 K for 30 min. Peaks ascribed to C, Si, Cr, Mn and Fe are marked in red, gray, pink, green and yellow, respectively. (b and c) Mass spectra for ferrite and cementite, respectively. Note the presence of the peak of 24.5 Da only in the cementite.

pulse fraction and evaporation rate [33]. It might be possible that the different material states (e.g. deformed and annealed) also influence the ratio of field-evaporated carbon molecules. As C_2^+ mainly contributes to the peak at 24 Da according to the peak deconvolution analysis, this peak was assigned as C_2^+ for atom maps of the annealed samples.

3. Results

3.1. Evolution of tensile strength upon annealing

Fig. 2 shows the tensile strength as a function of the annealing temperature. At room temperature the as-deformed material exhibits a tensile strength of 6.35 GPa, which, to the best of our knowledge, makes it the strongest pearlitic steel wire available today. The ultrahigh tensile strength remains after annealing at 423 K for 30 min. Beyond this temperature, the tensile strength decreases approximately linearly with the annealing temperature. The evolution of the tensile strength with annealing time shown in Fig. 3 indicates that the dramatic drop in tensile strength mainly occurs within the first 2–3 min of the annealing process. After this short time interval, the tensile strength remains approximately constant at a relatively low temperature of 523 K. Even for the highest temperature of 723 K, the tensile strength decreases only slightly with further annealing time. This suggests that the underlying structural changes take place during the early annealing stage. The large circles in Figs. 2 and 3 mark the annealing conditions under which the nanostructure and the distribution of alloy elements in the deformed and annealed wires were studied by APT and high-resolution (HR) TEM.

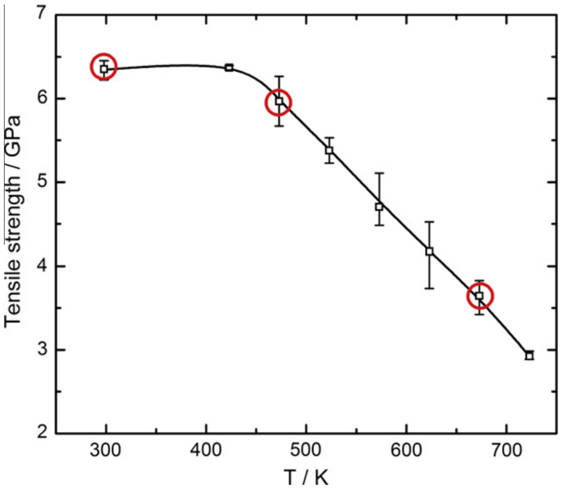

Fig. 2. Tensile strength as a function of annealing temperature for an annealing time of 30 min for cold-drawn hypereutectoid pearlitic steel wires. The red circles mark the annealing conditions for which APT measurements were performed.

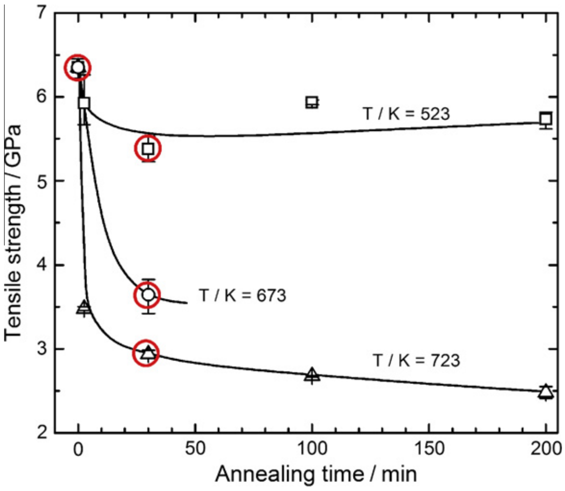

Fig. 3. Tensile strength as a function of annealing time at various temperatures for cold-drawn hypereutectoid pearlitic steel wires. The red circles mark the annealing conditions for which HRTEM studies were performed.

3.2. Evolution of microstructure upon annealing

APT results on the as-deformed and the 473 K and 673 K heat-treated states are displayed in Fig. 4. The atom maps of the as-deformed material (Fig. 4a) clearly show that a lamellar structure consisting of carbon-depleted (ferrite) and -enriched (cementite) regions still prevails after severe cold-drawing up to a strain of 6.02, although fragmentation of cementite lamellae can be observed. The lamellar structure remains stable after annealing at 473 K for 30 min (Fig. 4b). No cementite spheroidization occurs.

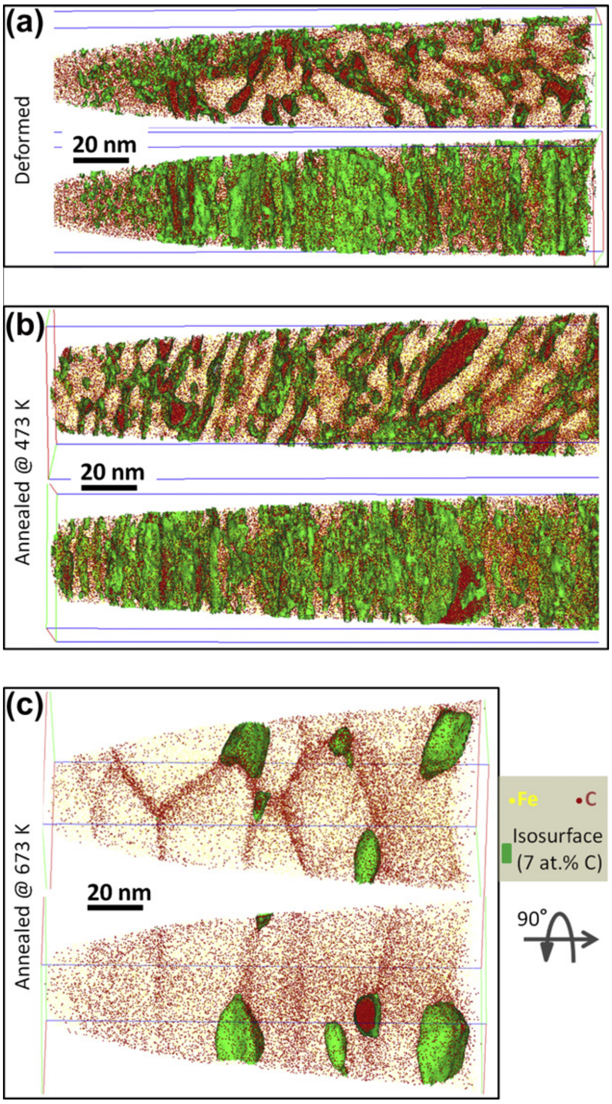

Fig. 4. 3-D carbon atom maps of hypereutectoid pearlitic steel wires with a cold drawing strain of $\epsilon = 6.02$: (a) as-deformed state; (b) annealed at 473 K for 30 min; and (c) annealed at 673 K for 30 min. The isoconcentration surfaces for 7 at.% carbon are shown in green. Only 30% of all carbon and 0.5% of all iron atoms are displayed. Both the cross-sectional (top) and longitudinal views (bottom) of the wires are shown.

However, Languillaume et al. observed speroidized cementite particles at 473 K [19]. Since the alloy elements, the initial strain and the annealing time of the pearlitic wire studied in Ref. [19] were different from those studied in this work, it is difficult to analyze the exact reasons for the different observations.

After heat treatment at 673 K for 30 min, strong microstructural changes occur. The original lamellar pearlitic structure is no longer visible; instead, a nearly equiaxed hexagonal (sub)grain structure has formed inside the ferrite (see Fig. 4c). The (sub)grain boundaries enclosing the carbon-depleted ferrite (sub)grains are decorated with carbon atoms. The (sub)grains exhibit an average grain size of 30–40 nm, which is about 2–3 times higher than the interlamellar spacing in the as-deformed wire [17,18]. Furthermore, the cementite lamellae have undergone spheroidization and are mainly located at the triple junctions. Similar observations were made by TEM for pearlitic steel wires at true drawing strains of 3.5 after annealing for 1 h at 823 K [19], 4.22 for 1 h at 673 K [9] and 5 for 0.5 h at 723 K [20]. Closer observation of Fig. 4c shows that the grains are not equiaxed but, rather, elongated along the drawing direction, with longitudinal sizes above 70 nm. It is noted that the reconstruction of the APT data shown in Fig. 4c was done based on the final tip radius after APT measurement, and is hence reliable. This observation suggests that the relatively coarse (sub)grain structure observed in the ferrite is not due to recrystallization, as this mechanism would lead to equiaxed grains.

Fig. 5 shows TEM micrographs of pearlitic wires for the corresponding conditions marked in Fig. 3. Strong strain contrast due to heavy drawing can be observed from Fig. 5a. The phase boundaries between ferrite and cementite are blurred and nearly invisible. The observation in the cross-section of the wire (Fig. 5b) shows the typical curled ribbon-like lamellar structure around the wire axis [3,34,35]. As explained by Hosford [36], the $\langle 1\,1\,0 \rangle$ fiber texture developed during wire drawing confines further slipping in each lamella to a plain strain state, and thus the compatibility of the neighboring grains can be maintained only by the bending of the grains around one another. This mechanism is referred to as curling [36–38]. The observation of fragmentation of cementite in Fig. 5b is consistent with the APT result shown at the bottom of Fig. 4a, where the cementite lamellae are curled and fragmented into numerous short segments and even small particles. This is direct evidence that cementite lamellae are capable of undergoing plastic deformation and even strain-induced fragmentation, as reported in Ref. [2,3]. Upon annealing at 523 K for 30 min, the lamellar structure is still preserved and no recrystallization occurs (Fig. 5c).

After annealing at 723 K (see Fig. 5d), the lamellar structure along the drawing direction is still visible, while cell/subgrain boundaries have formed in the ferrite and the cementite lamellae have undergone spheroidization. The ferrite cell/subgrains are elongated along the wire axis, in agreement with the APT observation at 673 K (Fig. 4c). In the direction perpendicular to the wire axis, the average subgrain size is below 80 nm.

3.3. Redistribution of carbon during annealing

Fig. 6 illustrates the carbon partitioning among the various phases or regions (ferrite, cementite and interface region) in the as-deformed and annealed samples, where the bulk carbon concentration is plotted against the cumulative (phase) volume fractions. In accordance with our previous works [17,18], the phases of ferrite and cementite, and the interface between them, are defined according to their carbon content (see also caption of Fig. 6), where the volume fraction of each phase can be estimated as the ratio of the total number of atoms in each phase to the total

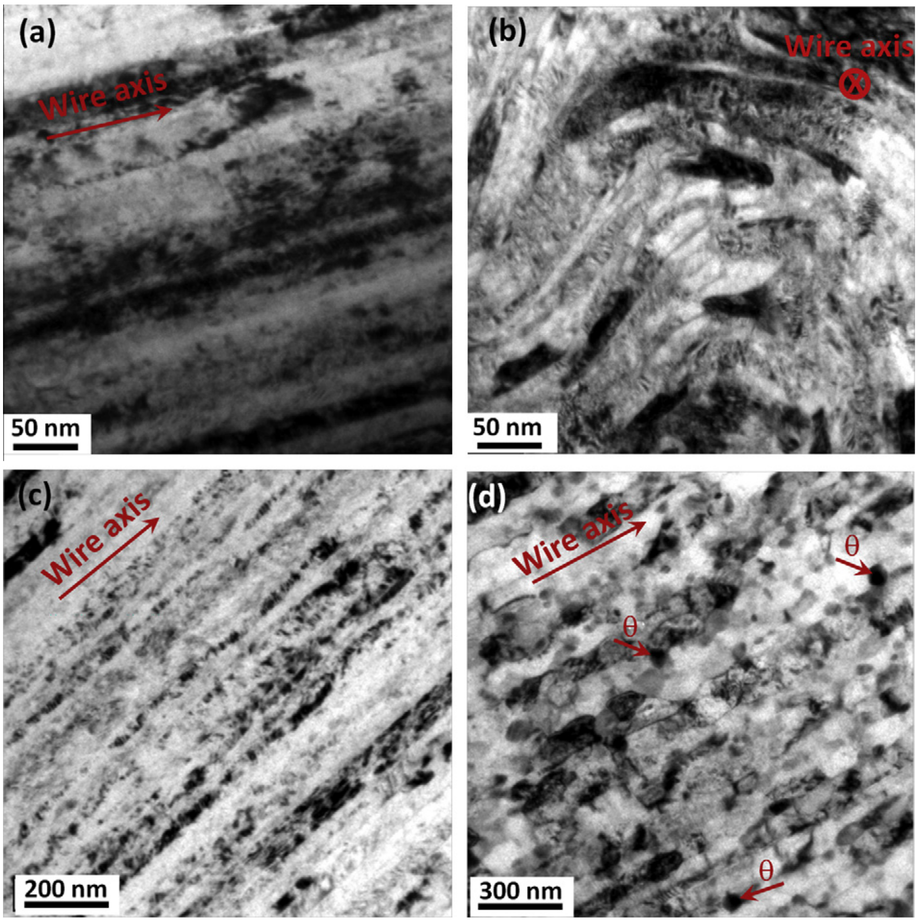

Fig. 5. TEM images of hypereutectoid pearlitic steel wires. (a and b) As-deformed ($\epsilon = 6.02$) states in longitudinal and transverse cross-sections of wires, respectively. (c and d) As-annealed states at 523 and 723 K for 30 min, respectively. The arrows mark the wire axis which is also parallel with the ferrite/cemetite interfaces. Some globular cementite particles (θ) are marked.

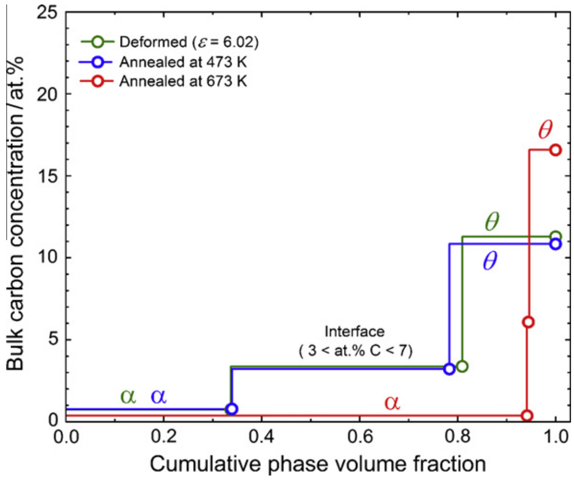

Fig. 6. Bulk carbon concentrations in the defined phase zones vs. volume fractions of the corresponding phase zones. Ferrite (α) and cementite (θ) are defined as the regions with carbon concentrations lower than 3 at.% and higher than 7 at.%, respectively. The region between the two phases is defined as the ferrite/cementite interface.

number of atoms in the whole sample. The result shows that, in the as-deformed sample, the carbon concentration of 0.73 ± 0.006 at.% in the ferrite is far beyond the equilibrium value of several tens of atom ppm, while the carbon concentration in the cementite decreases to approximately half of the stoichiometric value. In addition, the large volume fraction of the interface characterized by an extended carbon concentration gradient suggests dissolution of carbon atoms from cementite to ferrite and a mechanical alloying process. After annealing at 473 K for 30 min, no significant redistribution of carbon atoms is found, since both the carbon concentrations and the volume fractions of all phases remain close to the values measured in the as-deformed sample.

A dramatic change in the redistribution of carbon occurs after annealing at 673 K for 30 min. As shown in Fig. 6 (red curve), the high volume fraction of the ferrite/cementite interface produced during extreme deformation decreases greatly after annealing. The bulk carbon concentration in ferrite is reduced to 0.37 ± 0.003 at.% and the carbon concentration in the cementite of 16.6 ± 0.013 at.% approaches the stoichiometric value. We observe that the volume fraction of ferrite after annealing at 673 K even exceeds the value of 85% (for C wt.% = 0.98), as expected from the lever rule. This is due to the fact that a limited size of the probed volume confines the statistics in determining the phase volume fractions. However, this limit has little influence on the accuracy of the concentration measurement in each individual phase region.

Note that 16.6 at.% is not the carbon concentration in the center of the cementite particles, but the average one in the defined region (see caption of Fig. 6). As will be shown in Section 3.4, the carbon concentration inside these particles reaches 25 at.% after annealing at 673 K for 30 min. Both the dark-field image and the HRTEM result shown in Fig. 7 demonstrate the crystallinity of the cementite particle that may form during annealing at $T \geqslant 673$ K. However, its transformation mechanism upon high-temperature annealing is complicated in the present case due to the uncertainty of the existence of lamellar cementite before annealing. If the cementite undergoes only a partial chemical (not structural) decomposition before annealing, then the formation of cementite particles upon annealing proceeds without nucleation; instead, it is driven simply by the reduction of the ferrite/cementite phase boundary area.

3.4. Grain boundary excess of carbon after annealing at 673 K

Fig. 4 shows that carbon atoms segregate at the ferrite (sub)grain boundaries at 673 K. By using the sub-cutting method [17], the average carbon concentration inside the ferrite grains was measured to be 0.163 ± 0.057 at.% (see the dotted lines in Fig. 8f and g), while it exceeds 1.5 at.% at the grain boundaries (Fig. 8f and g). Two regions of interest cutting through the spheriodized cementite are selected for the analysis of the carbon concentration. The measured values of about 25 at.% C (Fig. 8h and i) show that the carbon concentration in cementite has reached the stoichiometric value again.

It is known that segregation of solute atoms at grain boundaries decreases the grain boundary energy, as described by the Gibbs adsorption isotherm [39–41],

$$d\gamma = -\Gamma_A d\mu_A \qquad (1)$$

where γ is the specific grain boundary energy, Γ is the excess amount of A atoms at the boundary and μ_A is the chemical potential of the solute atoms of type A. This means that the higher the solute excess at the grain boundary, the lower the grain boundary energy.

$\Gamma^{\alpha}_{C,gb}$, the grain boundary excess of carbon, can be determined either from 1-D concentration profiles (e.g. Fig. 8f and g) or by direct counting of the number of carbon atoms per grain boundary area. With the former method, the carbon concentration in (sub)grain interiors (as shown by the dotted lines in Fig. 8f and g) is subtracted from the measured concentrations. Using the latter method, the number of carbon atoms within the selected region, e.g. "GI" in Fig. 8a, is subtracted from the number of carbon atoms in region "GB", which has the same size as the domain "GI". By using the two methods, $\Gamma^{\alpha}_{C,gb}$ is determined to be (5.30 ± 0.73) atoms nm^{-2} (8.80×10^{-6} mol m^{-2}) and (5.14 ± 0.72) atoms nm^{-2} (8.54×10^{-6} mol m^{-2}), respectively.

According to Eq. (1), a carbon excess of $\approx 9 \times 10^{-6}$ mol m^{-2} reduces the grain boundary energy and thus reduces the driving force for grain coarsening, even when annealing the heavily cold-drawn pearlitic steel sample at 723 K. The stabilization of defects such as grain boundaries and dislocations by solute segregation, known as the defactant concept [39–41], has also been reported in Refs. [42–45].

3.5. Redistribution of Si, Mn and Cr during annealing at 673 K

Fig. 9a–d shows the atom maps of Si, Cr, Mn and C (as a reference), respectively, in the wire annealed at 673 K for 30 min. To quantify the distribution of the solute atoms, concentration profiles along a domain $10 \times 2 \times 83$ nm^3 in size, as shown in Fig. 9d, were plotted in Fig. 9f. Corresponding atom maps within the inspected region are shown in Fig. 9e. In accordance with the carbon distribution shown in Fig. 9e, the carbon concentration reaches a maximum in the center of a cementite particle and at the grain boundaries in ferrite, respectively, and has a minimum in the grain

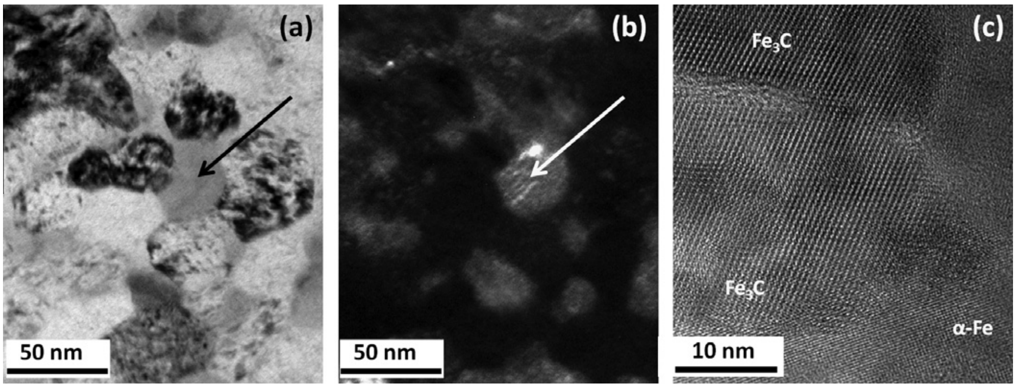

Fig. 7. (a) TEM bright-field and (b) dark-field images in the transverse cross-section of a hypereutectoid pearlitic wire after annealing at 673 K for 30 min. A distinct contrast line in the form of bright lines in one cementite particle marked with an arrow indicates a crystalline particle. (c) HRTEM image of a wire after annealing at 723 K for 30 min, showing a crystalline cementite particle in the ferrite matrix.

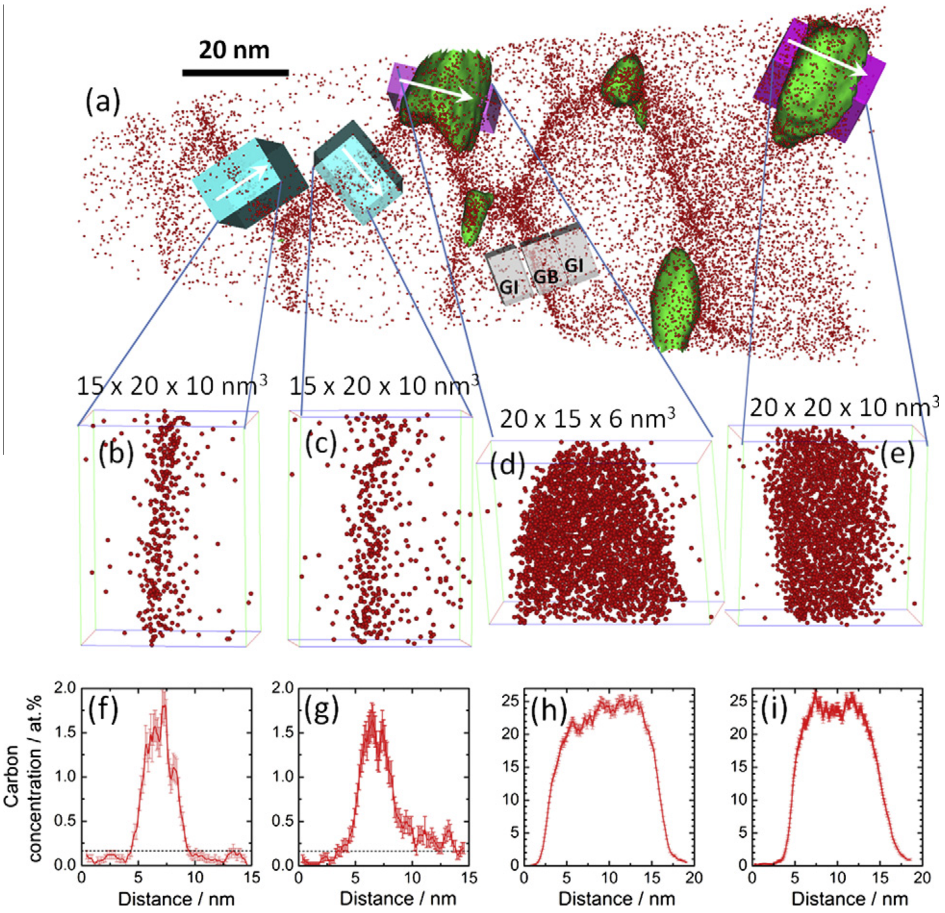

Fig. 8. (a) Carbon atom map of the annealed (673 K for 30 min) hypereutectoid pearlitic steel wire with selected regions of interest (ROIs). The white arrows mark the directions along which the concentration profiles are drawn. The gray-colored ROIs containing grain boundary (GB) and grain interior (GI) are shown as an example for determining the grain boundary excess of carbon (see text). (b–e) Carbon atom maps for the ROIs. The corresponding 1-D carbon concentration profiles are displayed below each atom map (f–i).The average carbon concentration inside the ferrite grains is displayed as short-dashed lines in (f) and (g).

interior (see Fig. 9e). Si is also segregated at the subgrain boundaries (see Fig. 9a and f), where the maxima and minima of the Si concentration correspond well to the locations of subgrain boundaries and subgrain interiors, respectively. The absolute minimum of Si at the center of the cementite particle is consistent to the diminishing equilibrium solubility of Si in cementite as calculated by Thermo-Calc (see Table 1). Cr and Mn atoms are strongly segregated in cementite (see Fig. 9b, c and e). In the grain interior we also observed a depletion of Cr and Mn atoms next to some subgrain boundaries (see the arrows in Fig. 9c). This suggests twofold kinetics in the redistribution of the alloy elements during annealing. One process is the diffusion of Cr and Mn atoms from the subgrain interior to the subgrain boundary inside the ferrite, which leads to Cr- and Mn-depleted areas next to the subgrain boundaries. In the second process, the subgrain boundaries supply a fast diffusion path along which Cr and Mn atoms can quickly diffuse to triple-junction lines, where the spheroidized cementite particles are located owing to the higher vacancy flux along subgrain boundaries. In addition, the distribution of Cr and Mn atoms in cementite is also inhomogeneous (see Fig. 9b, c and e top). The concentration profiles of Cr and Mn in Fig. 9f show a double plateau (see arrows), located at the ferrite/cementite phase boundaries.

4. Discussion

4.1. Thermal stability of microstructure and strength upon annealing below 473 K

The ultrahigh strength remained stable after the material was annealed at temperatures below 473 K for 30 min (see Fig. 2). This observation is consistent with the analyses of the as-deformed and annealed wires by APT (see Fig. 4a and b). The TEM image in Fig. 5c shows that the lamellar structure still remains even after annealing at 523 K. We conclude that no substantial microstructural change has taken place during annealing at temperatures below 473 K.

One can argue that some softening might already occur due to a slight recovery at the relatively low annealing temperatures. However, this could be compensated by static strain aging during low-temperature annealing or even during the storage of the cold-deformed material at room temperature. The net effect from these two phenomena is that the strength remains unchanged. This argument can

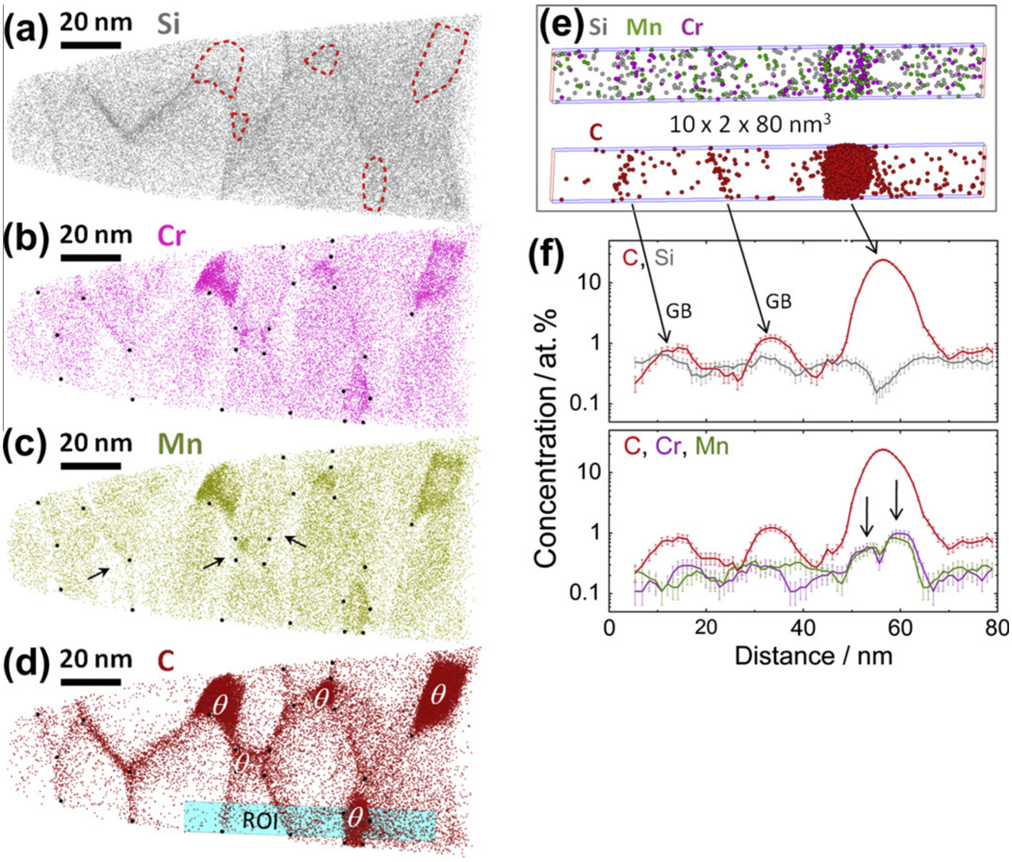

Fig. 9. 3-D atom maps of Si, Cr, Mn and C of a sample annealed at 673 K. 100% of Si, Cr and Mn and 30% of the carbon atoms are displayed. Cementite is labeled with "θ". The red dashed borders in (a) and the black dots in (b) and (c) mark cementite particles and grain boundaries shown in (d), respectively. The 1-D concentration profiles along the ROI chosen in (d) are shown in (f).

Table 1
Solubilities of Si, Mn and Cr in ferrite and cementite under equilibrium conditions calculated by Thermo-Calc using the nominal composition of the wire given in Section 2 (unit: at.%).

Temperature (K)	Si		Mn		Cr	
	Ferrite	Cementite	Ferrite	Cementite	Ferrite	Cementite
473	0.46	0	1.39×10^{-3}	1.81	1.37×10^{-4}	1.24
673	0.46	0	1.86×10^{-2}	1.73	3.27×10^{-3}	1.225

be further discussed as follows: before measuring the tensile strength (both at room temperature and after the various heat treatments), the as-cold-drawn wires were kept at room temperature for about 6 months. The carbon diffusion distance can be estimated as $x = \sqrt{6Dt}$ by taking the bulk diffusivity $D^{C}_{\alpha} = D^{C}_{0,\alpha} \cdot \exp\left(\frac{-Q}{RT}\right)$ ($D^{C}_{0,\alpha} = 2 \times 10^{-6}$ m^2 s^{-1} and $Q = 84.1$ kJ mol^{-1} [46], R is the gas constant) of carbon in ferrite. This rough estimate yields a carbon diffusion distance of 650 nm in ferrite at room temperature for $t = 0.5$ year and an additional 300 nm at 423 K for 30 min. This estimate shows that carbon can diffuse to dislocations within the fine ferrite lamellae. However, our recent results show that strain aging becomes less significant with increasing wire strain. For a true strain of 6.02 the strain aging effect is barely noticeable. This means that for weakly drawn wires some carbon atoms have not diffused sufficiently to decorate dislocations even after a storage period of 6 months at room temperature. However, they can diffuse to dislocations upon annealing for only 30 min. This implies an overestimation of the carbon diffusion length at room temperature, possibly due to the supersaturation of the ferrite with carbon upon cold drawing. We attribute the absence of strain aging upon high-temperature annealing for highly strained pearlitic wires ($\epsilon > 5$) to the slightly higher temperature that occurs during drawing as compared to weakly strained wires. This effect facilitates the strong segregation of carbon to single dislocations in the case of highly strained ferrite during the drawing process [17,18]. The effect limits the free sites at dislocations that remain for carbon decoration during static storage at room temperature or annealing at elevated temperatures. Moreover, the density of single dislocations decreases with further drawing due to the formation of ferrite dislocation cell/substructures which are also decorated with carbon [17,18].

4.2. Recovery and recrystallization during annealing above 473 K

Both the APT (Fig. 4c) and TEM (Fig. 5d) observations show that the elongated ferrite grains inherited from cold drawing still exist after annealing at 673 and 723 K for 30 min. These results suggest that no recrystallization occurs, since recrystallization typically yields equiaxed grains. Furthermore, after annealing at 673 K for 30 min, the carbon content in the ferrite amounts to 40 times the equilibrium value of 0.001 wt.% C at room temperature. This indicates an existence of lattice defects such as vacancies, dislocations and (sub)grain boundaries in the ferrite because these types of defects are able to supply additional sites to trap a large amount of carbon atoms [14,17,18,21]. This means that a typical entirely defect-free recrystallized structure has not yet been formed after annealing at 673 K for 30 min. In addition, the slight (sub)grain structure coarsening in ferrite indicates that recovery rather than recrystallization takes place during annealing because the observed grain size remains far below the typical recrystallized grain size, which is in the micrometer range.

The inhibition of recrystallization in the most heavily cold-deformed ($\epsilon = 6.02$) pearlitic wire can be attributed to the strong fiber texture [3,35], which reduces the driving force for recrystallization and decreases the mobility of grain boundaries by forming low-angle grain boundaries (one dominant grain orientation). Embury and Fisher [2] reported that the misorientation between the ferrite cells is of the order of 1° at a true drawing strain of 3.1. Tarui et al. [47] also confirmed the formation of a cell structure in the ferrite of pearlite at $\epsilon = 4.2$ by selected-area electron diffraction. In addition, the segregation of carbon at the cell/subgrain boundaries and the spheroidized cementite may also inhibit the recrystallization by reducing the grain boundary energy and pinning the grain boundaries against migration, respectively. Also, primary recrystallization proceeds through a nucleation and growth sequence, and the confined interlamellar spacing might be too small for a critical nucleus size to be reached. Thus, we suggest that the formation of cell/subgrain structures after annealing at temperatures above 473 K results not from recrystallization, but from strong recovery of the deformed microstructure.

4.3. Softening during annealing above 473 K

Based on the discussion above, the dramatic drop in tensile strength upon annealing at temperatures above 473 K seems to be mainly due to static recovery of the deformed microstructure through annihilation, rearrangement or polygonization of ferrite dislocations. Readers are referred to Ref. [18] for the mechanism of formation of (sub)grain structure inside the ferrite channel. In addition, the other microstructural changes upon annealing, such as cementite spherodization, redistributions of alloy elements, recovery of point defects (vacancies and interstitials) and relatively slight coarsening of cell/subgrain structures, may also cause the drop in tensile strength, as discussed below in more detail.

4.3.1. Recovery of dislocations at cell/subgrain boundaries

Severe plastic deformation such as cold drawing introduces a high dislocation density into the material. Recently, Zhang et al. [48] reported that the dislocation density ρ in the ferrite lamellae increases from $7.5 \times 10^{13}\ \mathrm{m}^{-2}$ in the as-patented state to $2 \times 10^{16}\ \mathrm{m}^{-2}$ after a cold-drawing strain of 3.68. Chen and Kirchheim [49] measured the dislocation density in an annealed pearlitic (0.8 wt.% C) steel wire produced by cold drawing to $\epsilon = 3$. They found that the dislocation density decreases to $8.53 \times 10^{14}\ \mathrm{m}^{-2}$ after annealing at 723 K for 30 min. While it is not clear how the recovery process occurs, it is very likely in the current system that dislocation recovery takes place mainly at the ferrite/cementite interfaces. For the materials studied in the present work, the lamellar spacing decreases to about 10 nm, thus the major portion of the dislocations created during cold drawing becomes stored at the interface between ferrite and cementite, where they form cell/grain boundaries superimposing on the phase boundaries [18]. Meanwhile, due to the decomposition of cementite, the dislocations from neighboring ferrite may meet at the sites of the original cementite and form a dipolar configuration. Together with an enhanced diffusion process along the phase interface due to severe plastic deformation, a fast annihilation of the dislocation dipoles during annealing becomes feasible. One may note that the quick drop of the tensile strength in the first few minutes during annealing agrees well with the feature of dipole annihilation, as suggest by Hausselt and Blum [50]. We estimate the reduction of the dislocation density on the basis of the drop of the tensile strength by calculating the change of the athermal stress due to the dislocations after annealing:

$$\Delta\sigma_{\mathrm{G}} = \alpha M G b \left(\sqrt{\rho_0} - \sqrt{\rho(T,t)} \right) \tag{2}$$

where α is the dislocation interaction constant, M is the Taylor factor, G is the shear modulus at ambient temperature, b is the length of the Burgers vector, ρ_0 is the dislocation density for the as-deformed state and $\rho(T,\ t)$ is the dislocation density for the as-annealed state. As a first estimate, we use $\alpha = 0.35$, $M = 3.06$, $G(300\ \mathrm{K}) = 8.2 \times 10^4\ \mathrm{MPa}$ [51] and $b = 0.25$ nm, and the dislocation densities of the above-mentioned measurements. This yields a reduction of the athermal stress of 2.5 GPa by taking the measured dislocations densities of $2 \times 10^{16}\ \mathrm{m}^{-2}$ for as-deformed wire [48] and $8.53 \times 10^{14}\ \mathrm{m}^{-2}$ for the wire annealed at 723 K for 30 min [49]. We ignore the possibility of relaxation of the dislocation stress field due to the segregation of carbon atoms at dislocation cores. While this value explains a major part of the strength reduction of 3.4 GPa at 723 K (Fig. 2), one should also consider possible effects associated with other microstructural changes.

4.3.2. Cell/subgrain coarsening during annealing

In the preceding section we discussed that the reduction of strength during annealing can be explained in terms of recovery of dislocations at cell/grain boundaries. As demonstrated by Blum and Zeng [52], the dislocation density in ultrafine-grained materials is closely related to the grain size since dislocations are mainly stored at grain boundaries. Here, as an alternative approach, we may directly describe the relationship between the strength and the (sub)grain size. From Figs. 4 and 5, the initial (sub)grain size d_0 can be roughly estimated to be 10 nm, and the size values $d(T)$ in the transverse direction of the wires are about 30 and 70 nm after annealing at 673 and 723 K, respectively. The corresponding strengths before (σ_0) and after (σ_T) annealing read 6.35, 3.64 and 2.92 GPa (see Fig. 2), respectively. The annealing apparently leads to coarsening of the grain structure, which consequently degrades the strength of the material. These data can be approximated by a Hall–Petch-type relationship:

$$\sigma_0 - \sigma_T = k_{H-P}\left(d_0^{-0.5} - d(T)^{-0.5}\right) \quad (3)$$

with $k_{H-P} \approx 550$ MPa $\mu m^{0.5}$. It has been frequently reported that the Hall–Petch slope in steels increases with the carbon concentration [53], in particular with the carbon concentration at grain boundaries [54–57]. Although a direct comparison of the carbon concentration-dependent k_{H-P} values between our measurement and the literature data is difficult because of the large scatter of the latter data sets [54–57], our measured value falls reasonably within the commonly observed range of $k_{H-P} = 315 \sim 760$ MPa $\mu m^{0.5}$ for steels with carbon segregation at ferrite grain boundaries [55,58].

4.3.3. Spheroidization of cementite

Steels containing pearlitic microstructures have higher strength and hardness than those with spherical cementite because the latter materials have a smaller area fraction of heterointerfaces. In the present case, it is hard to quantify the reduction of tensile strength resulting from the loss of phase boundary density due to cementite spheroidization. During annealing at temperatures above 473 K, the reduced phase boundaries are replenished by cell/subgrain boundaries. The question arises how effective the cell/subgrain boundaries are as barriers to dislocation motion. Together with the spheroidization of cementite, the ferrite cell/subgrain structure continuously coarsens during annealing. Hence, it is difficult to distinguish the softening effects resulting from the loss of phase boundaries from that associated with coarsening of the cell/subgrain structure. The estimate shown in Section 4.3.2 indicates the importance of the cell/subgrain size in the ferrite for the strength of pearlite.

4.3.4. Reduction of solid solution hardening

The loss of solid solution hardening due to the transport of solute atoms from the ferrite to the (sub)grain boundary as well as to cementite during annealing also leads to softening. A loss of carbon solid solution hardening between 300 and 673 K can be estimated by

$$\Delta\sigma_{sol} = k\left(\sqrt{C_{300}} - \sqrt{C_{673}}\right) \quad (4)$$

where k is a prefactor ($\approx 1.12 \times 10^4$ MPa for carbon in Fe [59]) and C_{300} and C_{673} are the carbon concentrations in weight percent in the ferrite after annealing at 300 and 673 K, respectively, for 30 min. Based on the values of 0.75 at.% (0.167 wt.%) for C_{300} and 0.16 at.% (0.036 wt.%) for C_{673} measured by APT, $\Delta\sigma_{sol}$ amounts to only 240 MPa. This means that the loss of solid solution hardening due to the redistribution of carbon atoms upon annealing does not play a major role in the reduction of the tensile strength.

The strengthening effect of other alloying elements, like Mn and Cr, is even lower than that of carbon in the ferrite. Therefore, significant softening resulting from the loss of solid solution hardening by Mn and Cr is not expected. On the contrary, these two elements may have a strengthening effect during annealing, as they are found to segregate at the interfaces between ferrite and cementite, and thus suppress the further growth of cementite particles during annealing. Regarding the solid solution effect, Si is known to be even less effective than Mn. Except for its segregation at ferrite gain boundaries, the distribution of Si in the ferrite and cementite upon annealing does not show a significant difference from that in the as-deformed wire (Fig. 10b).

4.4. Redistribution of alloy elements upon annealing

To better understand the elemental redistribution processes during annealing, proximity histograms [32,60] across ferrite/cementite interfaces were analyzed. Fig. 10 shows the proximity histograms of C, Si, Cr and Mn averaged over multiple interfaces in the as-deformed and annealed wires.

As the concentration profiles show little difference before (i.e. the as-deformed state) and after annealing at 473 K, we only compare in more detail the results between the as-deformed state and the state after annealing at 673 K. In the as-deformed state, two effects of the severe deformation on the microstructure can be observed. One is the partial redistribution of carbon from cementite into ferrite; the other is the approximately homogeneous distribution of Cr and Mn among ferrite and cementite compared to the equilibrium values (Table 1), which we attribute to mechanical mixing (see the green curves in Fig. 10(c) for Cr and (d) for Mn). The main reason why Si does not undergo mechanical mixing upon deformation is the insolubility of Si in cementite (see Table 1). In addition, Si is preferentially located at the ferrite grain boundaries, as seen in Fig. 9aa. This might render mechanical mixing phenomena more sluggish.

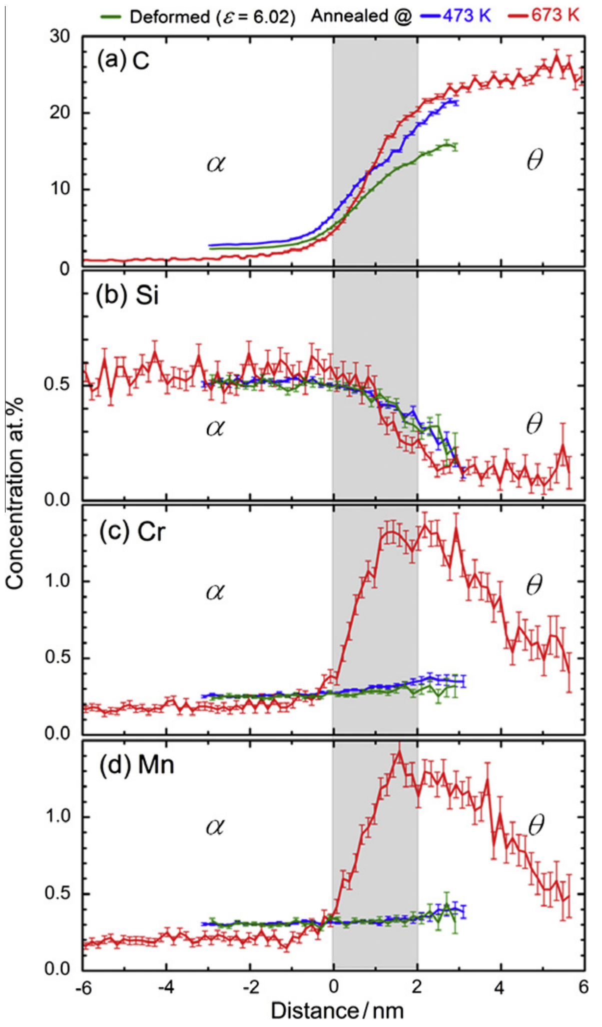

Fig. 10. The proximity histograms [32,60] of (a) C, (b) Si, (c) Cr and (d) Mn obtained from multiple interfaces shown in Fig. 4 for as-deformed (green) and as-annealed states at 473 K (blue) and 673 K (red). Ferrite and cementite separated by the interface (gray zone) are marked with α and θ, respectively.

After annealing at 673 K for 30 min, the alloy elements undergo strong redistribution. First, as shown in Fig. 10a, the reduced carbon content in cementite after deformation returns to the stoichiometric value. It should be mentioned that the carbon concentrations we found in cementite in the as-deformed state are inversely dependent on the thickness of the cementite lamellae [17]. The green curve shown in Fig. 10a is obtained from the analysis of relatively thick cementite lamellae. In addition, the concentration gradient at the interfaces between ferrite and cementite becomes sharper after annealing as compared to the blurred interface in the as-deformed state.

Second, a similar increase in the concentration gradient of Si at the ferrite/cementite interfaces indicates an enhanced redistribution of Si atoms from cementite to ferrite due to annealing (see Fig. 10b). It is noted that the concentration of Si increases monotonically from cementite to ferrite without any sign of enrichment of Si at the ferrite/cementite interface [9,61]. This may be attributed to a low initial Si content in cementite (in the as-deformed state) and the fast diffusivity of Si at ferrite grain boundaries, along which the Si can leave the cementite.

Third, a significant number of Cr and Mn atoms diffuse from ferrite to the interfaces between ferrite and cementite. It is known that Cr and Mn are carbide-forming elements and that their solubilities in cementite are much higher than in ferrite (Table 1), as they can substitute Fe in the carbides and form $(Fe,Cr)_3$ C and $(Fe,Mn)_3C$ [62,63], respectively. As a result, there is a driving force for Cr and Mn to diffuse from ferrite to cementite during annealing. However, the limited diffusivity of these atoms in cementite is likely to act as a kinetic barrier for the fast accommodation of the incoming atom flux from ferrite. According to Ref. [64], the diffusion coefficient of Mn in ferrite D_{α}^{Mn} ($2.4 \times 10^{-23}\ \mathrm{m}^2\ \mathrm{s}^{-1}$) is about three orders of magnitude higher than that in cementite D_{θ}^{Mn} ($8.8 \times 10^{-27}\ \mathrm{m}^2\ \mathrm{s}^{-1}$). According to Ref. [65], Cr behaves similarly to Mn. In particular, at ferrite grain boundaries the diffusivity of Cr and Mn can be even higher, so that the incoming atoms segregate at the ferrite/cementite interface and result in the concentration peaks we observe here (Fig. 10c and d). A similar scenario was recently reported for a maraging-TRIP steel, where the Mn partitioning at martensite/austenite interfaces is due to the low diffusivity of Mn in the austenite, which does not allow the incoming Mn flux from the adjacent martensite to be accommodated within the austenite [66,67].

5. Conclusions

The micro- and nanostructures of a heavily cold-drawn hypereutectoid pearlitic steel wire were studied by APT and TEM in both the as-deformed and annealed states. The lamellar structure consisting of ferrite and cementite is preserved up to annealing at 473 K, with only small changes in the distribution of the solute atoms. Upon annealing at 673 K, the lamellar structure transforms to a subgrain structure in ferrite, with carbon atoms segregated at the grain boundaries and spheroidized cementite located at the triple junctions inside the ferrite. No evidence of recrystallization was found after annealing up to 723 K. The atom maps and concentration profiles of the solutes suggest that (sub)grain boundaries provide a fast diffusion path, along which Si atoms can diffuse from cementite to ferrite and segregate at ferrite grain boundaries. Cr and Mn diffuse from ferrite to cementite, where a kinetic freezing effect (smaller diffusion coefficient in cementite) for the further diffusion of Cr and Mn deeper into the cementite leads to segregation of Cr and Mn at the phase boundaries between ferrite and cementite. The considerable drop in tensile strength after annealing can be mainly attributed to the recovery of dislocations and coarsening of dislocation substructures. The loss of solid solution hardening due to the redistribution of carbon atoms upon annealing gives only a small contribution.

Acknowledgements

The authors thank Dr. H. Yarita, from Suzuki Metal Industry Co., Ltd., for providing the cold drawn specimens. We also thank Dr. D. Ponge, from Max-Planck Institut für Eisenforschung, Prof. W. Blum, from University of Erlangen-Nürnberg, and Dr. J. Takahashi, from Nippon Steel Corporation, for many valuable discussions, and Dr. A. Kostka for performing TEM. We are grateful to the Deutsche Forschungsgemeinschaft for funding this research (SFB 602 and KI230/34-1).

References

[1] Takahashi T, Ochiai I, Tashiro H, Ohashi S, Nishida S, Tarui T. Nippon Steel Tech Rep 1995;64:45.
[2] Embury JD, Fisher RM. Acta Metall 1966;14:147.
[3] Langford G. Metall Trans A 1977;8:861.
[4] Embury JD, Hirth JP. Acta Metall Mater 1994;42:2051.
[5] Raabe D, Choi P, Li YJ, Kostka A, Sauvage X, Lecouturier F, et al. MRS Bull 2010;35:982.
[6] Belous MV, Cherepin VT. Fiz. Met Metalloved 1961;12:685.
[7] Gridnev VN, Gavrilyuk VG, Dekhtyar IY, Meshkov YY, Nizin PS, Prokopenko VG. Phys Status Solidi A 1972;14:689.
[8] Danoix F, Julien D, Sauvage X, Copreaux J. Mater Sci Eng A 1998;250:8.
[9] Hong MH, Reynolds Jr WT, Tarui T, Hono K. Metall Mater Trans A 1999;30:717.
[10] Sauvage X, Copreaux J, Danoix F, Blavette D. Philos Mag A 2000;80:781.
[11] Hono K, Ohnuma M, Murayama M, Nishida S, Yoshie A. Scripta Mater 2001;44:977.
[12] Wetscher F, Pippan R, Sturm S, Kauffmann F, Scheu C, Dehm G. Metall Mater Trans A 2006;37:1963.
[13] Goto S, Kirchheim R, Al-Kassab T, Borchers C. Trans. Nonferrous Met Soc China 2007;17:1129.
[14] Borchers C, Al-Kassab T, Goto S, Kirchheim R. Mater Sci Eng A 2009;502:131.
[15] Takahashi J, Tarui T, Kawakami K. Ultramicroscopy 2009;109:193.
[16] Sauvage X, Lefebvre W, Genevois C, Ohsaki S, Hono K. Scripta Mater 2009;60:1056.
[17] Li YJ, Choi P, Borchers C, Chen YZ, Goto S, Raabe D, et al. Ultramicroscopy 2011;111:628.
[18] Li YJ, Choi P, Borchers C, Westerkamp S, Goto S, Raabe D, et al. Acta Mater 2011;59:3965.
[19] Languillaume J, Kapelski G, Baudelet B. Acta Mater 1997;45:1201.
[20] Borchers C, Chen Y, Deutges M, Goto S, Kirchheim R. Philos Mag Lett 2010;90:581.
[21] Takahashi J, Kosaka M, Kawakami K, Tarui T. Acta Mater 2012;60:387.
[22] Cerezo A, Godfrey TJ, Smith GDW. Rev Sci Instrum 1988;59:862.
[23] Blavette D, Deconihout B, Bostel A, Sarrau JM, Bouet M, Menand A. Rev Sci Instrum 1993;64:2911.
[24] Miller MK, Cerezo A, Hetherington MG, Smith GDW. Atom probe field ion microscopy. Oxford: Oxford University Press; 1996.
[25] Kelly TF, Miller MK. Rev Sci Instrum 2007;78:031101.
[26] Seidman D. Annu Rev Mater Sci 2007;37:127.
[27] Marquis EA, Miller MK, Blavette D, Ringer SP, Sudbrack CK, Smith GDW. MRS Bull 2009;34:725.
[28] Pereloma EV, Stohr RA, Miller MK, Ringer SP. Metall Mater Trans 2009;40A:3069.
[29] Miller MK. Rev Sci Instrum 2007;78:031101.
[30] Miller MK, Russell KF. Surf Interface Anal 2007;39:262.
[31] Kelly TF, Miller MK. Microsc Res Tech 2006;69:359.
[32] Miller MK, Forbes RG. Mater Charact 2009;60:461.
[33] Takahashi J, Kawakami K, Kobayashi Y. Ultramicroscopy 2011;111:1233.
[34] Langford G. Metall Trans 1970;1:465.
[35] Zelin M. Acta Mater 2002;50:4431.
[36] Hosford Jr WF. Trans AIME 1964;230:12.
[37] Raabe D, Heringhaus F, Hangen U, Gottstein G. Z Metallkd 1995;86:405.
[38] Heringhaus F, Raabe D, Gottstein G. Acta Mater 1995;43:1467.
[39] Kirchheim R. Acta Mater 2002;50:413.
[40] Kirchheim R. Acta Mater 2007;55:5129.
[41] Kirchheim R. Acta Mater 2007;55:5139.
[42] Boylan K, Ostrander D, Erb U, Palumbo G, Aust KT. Scripta Metall Mater 1991;25:2711.
[43] Mehta SC, Smith DA, Erb U. Mater Sci Eng A 1995;204:227.
[44] Farber B, Cadel B, Menand A, Schmitz G, Kirchheim R. Acta Mater 2000;48:789.
[45] Choi P, da Silva M, Klement U, Al-kassab T, Kirchheim R. Acta Mater 2005;53:4473.
[46] Wert CA. Phys Rev 1950;79:601.
[47] Tarui T, Maruyama N, Takahashi J, Nishida S, Tashiro H. Nippon steel technical report no. 91; January 2005.
[48] Zhang X, Godfrey A, Huang X, Hansen N, Liu Q. Acta Mater 2011;59:3422.
[49] Chen YZ, Kirchheim R. Personal communication.
[50] Hausselt J, Blum W. Acta Metall 1976;24:1027.
[51] Frost HJ, Ashby MF. Deformation-mechanism maps. Oxford: Pergamon Press; 1982.
[52] Blum W, Zeng XH. Acta Mater 2009;57:1966.
[53] Nam WJ, Bae CM, Lee CS. J Mater Sci 2002;37:2243.
[54] Wilson DV. Met Sci J 1967;1:40.
[55] Mintz B, He H, Smith GDW. Mater Sci Technol 1992;8:537.
[56] Takeda K, Nakada N, Tsuchiyama T, Takaki S. ISIJ Int 2008;48:1122.
[57] Takahashi J, Kawakami K, Ushioda K, Takaki S, Nakata N, Tsuchiyama T. Scripta Mater 2012;66:207.
[58] Mintz B. Met Technol 1984;11:265.
[59] Gottstein G. Physikalische grundlagen der materialkunde. Heidelberg: Springer-Verlag; 1998.
[60] Hellman OC, Vandenbroucke JA, Rüsing J, Isheim D, Seidman DN. Microsc Microanal 2000;65:437.
[61] Balak J, Sauvage X, Lee DL, Lee CY, Pareige P. Adv Mater Res 2007;26–28:45.
[62] Gurry RW, Christakos J, Darken LS. Trans ASM 1961;53:187.
[63] Schaaf P, Wiesen S, Gonser U. Acta Metall Mater 1992;40:373.
[64] Fridberg J, Trndahl LE, Hillert M. Jernk Ann 1969;153:263.
[65] Barnard SJ, Smith GDW, Garratt-Reed AJ, Vander Sande JB. In: Aaronson HI, Laughlin DE, Sekerka RF, Wayman CM, editors. Proceedings of the international conference on "solid–solid phase transformations". Warrendale (PA): AIME; 1982. p. 881.
[66] Raabe D, Ponge D, Dmitrieva O, Sander B. Scripta Mater 2009;60:1141.
[67] Dmitrieva O, Ponge D, Inden G, Millán J, Choi P, Sietsma J, et al. Acta Mater 2011;59:364.